Decomposition of TiH_2 studied in-situ by synchrotron X-ray and neutron diffraction

C Jiménez[1,2], F Garcia-Moreno[1,2], B Pfretzschner[1,2], M Klaus[2], M Wollgarten[2], I Zizak[2], G Schumacher[2], M Tovar[2] and J Banhart[1,2]

[1] Technische Universität Berlin, Hardenbergstr. 36, 10623 Berlin, Germany

[2] Helmholtz-Zentrum Berlin für Materialen und Energie, Hahn-Meitner-Platz 1, 14109 Berlin, Germany

Abstract

Decomposition during constant heating of as-received and pre-oxidised titanium hydride (TiH_2) powder in flowing and resting Ar was studied in-situ by synchrotron X-ray and neutron diffraction. Diffraction data were compared to corresponding thermoanalysis traces in order to relate peaks of H_2 release with individual phase transformations. We found that every peak of H_2 release is correlated with regimes of lattice parameters contraction. Core-shell models to describe the decomposition processes measured were found, and further verified by electron microscopy. The models show that a shell of the hcp hydrogen solid solution (α) around each particle core controls the dehydrogenation of the as-received TiH_2, while a TiO_2 rutile shell controls the outgassing from the pre-oxidised powder.

Keywords: TiH_2 decomposition, in-situ synchrotron XRD, blowing agent, core-shell model

1. Introduction

TiH_2 powder is the most widely used blowing agent for making metal foams either through powder metallurgical (PM) or melting routes [1]. It is also used for producing porous Ti for biomedical applications [2] and as a hydrogen storage medium [3]. Metal foams made by the PM route have more regular pore sizes if TiH_2 starts to release H_2 during melting of the alloy [4, 5]. Depending on the alloy used, TiH_2 is therefore commonly used either in the as-received condition or after pre-treatments. Prominent H_2 release accompanied by mass loss

from as-received TiH_2 starts at about 400 °C and peaks in various temperature regimes. After performing an oxidation pre-treatment, the onset temperature of TiH_2 can be shifted up to between 500 and 550 °C, and the H_2 release curve is modified to exhibit a single-peak [5 - 9]. Core-reacting models were applied to describe the oxidation process [9, 10] but the decomposition processes of both as-received and pre-oxidised TiH_2 powders are not yet fully understood. It is still unclear how the peaks of H_2 release are related to the phase transformations of TiH_2.

The combination of thermoanalysis with in-situ diffraction is appropriate for such investigations. Sandim et al. and Liu et al. studied the dehydrogenation of TiH_2 powder in this way [3, 11]. They performed detailed thermoanalysis but achieved a limited temperature resolution of 50 K for in-situ angle dispersive X-ray diffraction (AD-XRD) of CuK_α radiation from X-ray tubes. This resulted in misinterpretations of their diffraction data that led them to report incorrectly the phase transformation sequences. An additional drawback common to both studies was the use of different atmospheric conditions: inert gas flow for thermoanalysis and vacuum for in-situ XRD. This difference prevented a direct comparison of the results from the two methods because decomposition is significantly faster under vacuum than in flowing inert gas [12].

Energy dispersive X-ray diffraction (ED-XRD) of white synchrotron radiation in transmission geometry was used as the main method in this study because it allows for much higher acquisition rates than AD-XRD from X-ray tubes due to higher flux and simultaneous acquisition of diffractograms. This allowed for a temperature resolution of 2.9 K and a clearer insight into the phase transformation sequence of as-received TiH_2. In addition, disputed aspects of the sequence were clarified both with AD-XRD of monochromatic synchrotron radiation and in-situ neutron diffraction. The rationale of using 3 different diffractometers is to vary the probing depth of the radiation and the possibilities to adjust the atmospheric

conditions around the decomposing hydride. This study reports for the first time the phase transformation sequence of pre-oxidised TiH_2, and a correlation between phase transformation sequences and peaks of H_2 release. The spatial distribution of phases investigated by electron microscopy validated experimentally core-shell models for the decomposition of as-received as well as pre-oxidised TiH_2 powders under conditions of constant heating.

2. Experimental

2.1 Materials: as-received and pre-oxidised TiH_2 powder

We used TiH_2 powder supplied by Chemetall GmbH, Germany (PS grade, purity 98.8 %, nominally < 36 μm, D_{50} = 6 μm). We prepared pre-oxidised TiH_2 powder by heating 3 g of as-received powder in an alumina crucible inside an open horizontal tube furnace pre-heated to 480 °C. After 180 minutes, the crucible was withdrawn from the furnace and cooled down to ambient temperature.

2.2 Thermoanalysis and oxygen content analysis

Thermogravimetry and mass spectroscopy (TG-MS) were carried out simultaneously in a Netzsch STA 409 C, which is a thermobalance coupled via a skimmer to a quadrupole mass spectrometer. The precision of the thermobalance is 10^{-4} g. A blank measurement was performed on an empty alumina crucible heating at 10 $K \cdot min^{-1}$ from 35 to 1100 °C under flowing Ar gas. Before heating, the thermoanalyser was evacuated and back-filled with Ar twice. After the blank measurement, 200 mg of powder were poured into the crucible and TG-MS analysis was done applying the same temperature profile and atmosphere used for the blank. Oxygen contents were determined by carrier gas hot extraction in a Horiba EMGA 620 WC nitrogen/oxygen analyser on 5 mg powder [13].

2.3 Ex-situ AD-XRD

Powder AD-XRD of CuK_α radiation was performed ex-situ on as-received and pre-oxidised TiH_2 samples in a Bruker-AXS D8 Advance 2-circle diffractometer. These diffractograms were used for phase identification with the help of the International Center for Diffraction Data (ICDD-PDF) database. Lattice parameters were determined by Rietveld refinements using the software `FullProf`.

2.4 In-situ ED-XRD

The phase transformation sequences were followed in-situ by ED-XRD at the EDDI experimental station at the BESSY II synchrotron light source of the Helmholtz Centre Berlin. The powder sample was illuminated by a white beam of X-rays and the energy of diffracted photons was measured in transmission geometry at $2\theta = 8°$ by a multi-channel analyzing detector. Using this method, the whole diffracted spectrum is available at all times. Further details of the EDDI beamline are given in [14, 15]. For this study, an Anton Paar DHS 1100 furnace equipped with an X-ray transparent graphite dome was attached to the goniometer. Powder samples were poured into a thin cylindrical alumina crucible of 5 mm inner diameter into which a hole through the wall had been laser-drilled. After tightening the crucible to the heating plate, a thermocouple was slid through the hole to measure the sample temperature T_S. A second thermocouple measured the temperature of the heating plate T_H. The graphite dome closed the furnace chamber which was evacuated for 5 minutes using a mechanical pump and backfilled with Ar. An argon gas pressure of 1.2 bar at the inlet induced Ar flow through the chamber. The temperature was increased from 30 to 950 °C at 10 $K \cdot min^{-1}$, after which the heater was turned off and cooling took place. Additionally, as-received powder samples were heated from 30 to 950 °C at 5 $K \cdot min^{-1}$ in flowing Ar and at 10 $K \cdot min^{-1}$ but in resting Ar atmosphere. The latter was realised by closing the exhaust and gas inlet before heating. Data acquisition and temperature cycle were computer-controlled by the software package `Spec`. One spectrum was acquired every 17.4 s, thus the temperature

resolution for heating at 10 $K \cdot min^{-1}$ was 2.9 K. Preliminary in-situ diffraction experiments were carried out by AD-XRD and neutron diffraction. Two selected examples that contribute to the discussion of the results obtained by ED-XRD are included as Appendix B (AD-XRD) and Appendix C (neutron diffraction).

2.6 Electron microscopy

Scanning electron microscopy (SEM) was carried out using a Zeiss SUPRA VP operated at 10 kV accelerating voltage. Transmission electron microscopy (TEM) was performed in a Zeiss LIBRA 200 FE operated at 200 kV accelerating voltage. Bright-field images and electron diffraction patterns were obtained using a CCD camera. An in-column energy filter was employed to obtain zero-loss filtered bright-field (ZLFBF) images and selected area electron diffraction (SAED) patterns. Throughout the paper, SAED patterns are shown with inverted grey scale to improve visibility of faint diffraction features. The energy filter was also used for elemental mappings by acquisition of jump ratio images at the oxygen K-edge. For sample preparation, the powders were mixed with an epoxy resin containing carbon nanoparticles. After curing, slices were cut and then reduced to 8 μm thickness by mechanical grinding and polishing. Final thinning was done by ion milling.

3. Results

3.1 Phases before heating

As-received TiH_2 is cubic, belonging to the F$m\bar{3}m$ space group (s.g.) in which the Ti atoms form a face centred cubic (fcc) arrangement and the hydrogen atoms sit on the tetrahedral sites. The diffractogram was compatible with $TiH_{1.924}$ (PDF#25-0982 of the ICDD database) and the Rietveld-refined parameter was a = 4.4509 ± 0.0004 Å.

After oxidation pre-treatment, the hydride peaks moved to higher 2θ values and peaks of TiO_2 rutile and Ti_3O appeared. The refined lattice parameter of the hydride after

pre-treatment was a = 4.4171 ± 0.001 Å. TiO_2 rutile belongs to the tetragonal s.g. $P4_2/mnm$ with lattice parameters a = 4.593 Å and c = 2.958 Å (PDF#75-1757). Ti_3O is trigonal (PDF#72-1806), its s.g. $P3\bar{1}c$ is and its lattice parameters are a = 5.15 Å and c = 9.56 Å, respectively.

3.2 Mass loss and H_2 release vs. temperature

Mass loss Δm and specific mass = 2 ion current (i.e. mass = 2 ion current divided by the initial sample mass) I_2 vs. temperature for as-received and pre-oxidised TiH_2 powders are given in Fig. 1. I_2 is a measure of the H_2 release rate, whereas the mass loss is the corresponding cumulative value. Both curves provide complementary information, but for simplicity hereafter we refer to the I_2 curve as the H_2 release curve. Δm was used to determine the H concentration (C_H) in the powder. Onset temperatures of H_2 release were defined by two intersecting tangents as shown in the inset of Fig. 1. As-received TiH_2 started to release H_2 from 220 °C followed by a small peak at 330 °C, accompanied by negligible mass loss only. Above the onset temperature of 375 °C, mass loss regimes were correlated with peaks of H_2 release at 439, 486 and 607 °C. A kink was observed at 780 °C, after which the H_2 release slowed down and ceased at 960 °C. The total mass loss from the as-received powder was 3.8 wt.%. Pre-oxidised TiH_2 had a first onset at 461 °C and a second at 535 °C followed by a single-peak at 647 °C, after which H_2 evolution declined and ended at about 890 °C. The total mass loss from the pre-oxidised powder was 2 wt.%.

3.3 Phase transformation sequences

3.3.1 As-received powder

Results from the in-situ ED-XRD experiments are given as density maps of intensities containing the diffraction lines of phases dispersed in energy vs. time in Fig. 2. In Fig. 2a, the diffraction lines of the δ, α and β phases in as-received powders evolved in time and temperature under Ar flow. Legends “first” and “last” indicate at what temperature phases

appeared and vanished. The starting phase was δ. As temperature increased, the two hydrogen-containing solid solutions α and β appeared. The α phase is hexagonal close packed (hcp, s.g. $P6_3mmc$), β is body centred cubic (bcc, s.g. $Im\bar{3}m$) and hydrogen atoms sit randomly on the tetrahedral sites of both phases [16]. For simplicity, we often refer to these three phases as δ, α and β. The sample temperature T_S (t) was measured at the height of the diffracting volume located about 1.5 mm above the heating plate and deviated from T_H(t) because heat conduction through the powder samples deteriorated with increasing temperature. Moreover, Ar flow enhanced the deviation of T_S(t) from T_H(t) since $T_{S\,max}$ was 807 °C under Ar flow but 880 °C in resting Ar atmosphere (compare Fig. 2a with b). Even though one spectrum was acquired every 2.9 K, systematic temperature differences of up to 15 K were detected for T_S at a given T_H on other samples. Temperatures indicated in the diffraction lines were extracted from the T_S(t) profile. Thus the phase transformation sequence extracted from Fig. 2a can be expressed as:

$$\begin{cases} \text{heating}: \delta \xrightarrow{432\,^\circ\text{C}} \delta+\alpha \xrightarrow{514\,^\circ\text{C}} \delta+\alpha+\beta \xrightarrow{536\,^\circ\text{C}} \alpha+\beta \xrightarrow{702\,^\circ\text{C}} \alpha \\ \text{cooling}: \text{no phase transformation } (\alpha \text{ remained}) \end{cases} \quad (1)$$

Sequence (2) was obtained, also under Ar flow but after reducing the heating rate from 10 to 5 K·min^{-1}. The effect was a shift by 27, 58, 44 and 59 K towards lower temperatures for each phase transformation.

$$\begin{cases} \text{heating}: \delta \xrightarrow{405\,^\circ\text{C}} \delta+\alpha \xrightarrow{456\,^\circ\text{C}} \delta+\alpha+\beta \xrightarrow{492\,^\circ\text{C}} \alpha+\beta \xrightarrow{643\,^\circ\text{C}} \alpha \\ \text{cooling}: \text{no phase transformation } (\alpha \text{ remained}) \end{cases} \quad (2)$$

Sequence (1) got strongly modified after changing the atmospheric conditions from flowing to resting Ar. In this case the phase transformation extracted from Fig. 2b was:

$$\begin{cases} \text{heating}: \delta \xrightarrow{448\,^\circ\text{C}} \delta+\alpha \xrightarrow{578\,^\circ\text{C}} \delta+\alpha+\beta \xrightarrow{620\,^\circ\text{C}} \alpha+\beta \xrightarrow{744\,^\circ\text{C}} \beta \\ \text{cooling}: \beta \xrightarrow{568\,^\circ\text{C}} \beta+\alpha \xrightarrow{264\,^\circ\text{C}} \beta+\alpha+\delta \xrightarrow{157\,^\circ\text{C}} \alpha+\delta \end{cases} \quad (3)$$

The first three phase transformations of sequence (3) were shifted to higher temperatures than their equivalents in sequence (1). However at 744 °C, a transformation from (α+β) into β occurred and during cooling three phase transformations resulted in the mixture (α+δ).

3.3.2 Pre-oxidised powder

Fig. 3 is the density map of diffracted intensities and temperature profiles for the pre-oxidised powder. The asterisk "*" in δ*, α* and β* denotes compositionally modified phases caused by the pre-oxidation, i.e. containing more O and less H. Beside this, the crystal structures were the same as of δ, α and β. This sample initially contained three phases: δ*, Ti_3O and TiO_2. Lines of Ti_3O matched the ones of α* (see e.g. O_{112} connected to α^*_{101} in Fig. 3). The transition from Ti_3O into α* at 500 °C was assumed because according to the Ti-O binary phase diagram Ti_3O is not stable above this temperature [17, 18]. Up to 500 °C the lines of all phases moved towards lower energies indicating lattice expansion, after which at 538 °C β* appeared and the lines of all phases shifted towards higher energies indicating lattice contraction. The diffraction lines of TiO_2 faded at about 623 °C (see r_{101} line). β* disappeared at 673 °C and α* was left as final phase. The phase transformation sequence of pre-oxidised TiH_2 therefore can be summarized as:

$$\begin{cases} \text{heating}: \delta^* + Ti_3O + TiO_2 \xrightarrow{500\,^\circ C} \delta^* + \alpha^* + TiO_2 \xrightarrow{538\,^\circ C} \delta^* + \alpha^* + \beta^* + TiO_2 \\ \qquad\qquad \xrightarrow{623\,^\circ C} \delta^* + \alpha^* + \beta^* \xrightarrow{630\,^\circ C} \alpha^* + \beta^* \xrightarrow{673\,^\circ C} \alpha^* \\ \text{cooling}: \text{no phase transformation } (\alpha^* \text{ remains}) \end{cases} \quad (4)$$

3.4 Powder morphology and spatial distribution of phases

3.4.1 As-received powder

The condition for the as-received powders is indicated in the sample temperature profile $T_s(t)$ in Fig. 2a as "before heating". Its morphology is shown in Fig. 4. The powder particles had flat surfaces, sharp edges and a broad size distribution which ranged from μm

sized particles (Fig. 4a) down to particles of about 100 nm diameter (Fig. 4b). The ring-shaped SAED pattern obtained for the region shown in Fig. 4b indicates that the as-received TiH_2 particles were polycrystalline. All rings could be indexed by d_{hkl} values of the δ phase only.

The initial microstructure evolved to the one shown in Fig. 5 after cooling from 430 °C (see T_s (t) in Fig. 2a). Fig. 5a is a ZLF bright-field image of a larger particle, which had been sliced for TEM. The microstructure of the central particle comprised two different parts: a homogeneous core and an outer shell consisting of small crystallites, which according to the indexed SAED patterns in Fig. 5b had the structure of the α phase. The core of the particle was single crystalline δ phase as confirmed by its [200] zone axis pattern (Fig. 5c).

After heating to 807 °C and subsequent cooling, the sample microstructure changed to the one shown in Fig. 6. The SEM image (Fig. 6a) shows sintering of the former powder particles, grain growth and residual porosity. Triple points of grain boundaries were marked by arrows in the bright field TEM image (Fig. 6b). The crystallographic structure of these large grains was identified as belonging to the α phase by electron diffraction (inset of Fig. 6b).

3.4.2 Pre-oxidised powder

Fig. 7a shows a cross-sectioned particle in the condition "before heating" as indicated in Fig. 3. Thickness variations led to varying contrast in the core. A small region of uniform contrast in the core was used for SAED and identified as δ* hydride phase (Fig. 7b). According to the ring-shaped SAED pattern shown in Fig. 7c the shell was a mixture of Ti_3O and TiO_2 oxides. The oxygen enrichment in the shell compared to the core was corroborated by the oxygen map given in Fig. 7d. After heating to 805 °C and cooling, see T_s (t) in Fig. 3, this sample remained a powder (Fig. 8a), i.e. no sintering had taken place. The SAED pattern

shown in Fig. 8b was obtained from the indicated region and corresponds to a [002] zone axis of the hcp α^* phase.

3.5 Oxygen content analysis

Oxygen content analysis conducted on samples "before heating" and "after cooling from $T_{S,max.}$" is summarized in Table 1. These values are the average of 3 measurements. Statistical scatter between measurements was about 3 % but systematic errors could be larger. These average values indicate oxygen uptake after heating to $T_{s\ max.}$, but the effect could be within the experimental error.

4. Discussion

4.1 Mass loss and H_2 release

The observation of a multi-peak structure of H_2 release from the as-received powder and of a single peak for pre-oxidised powder as shown in Fig. 1 confirms previous reports by other authors applying similar experimental conditions [3, 7 - 10]. The total mass loss of 3.8 % from the as-received powder agrees with reported values that range from 3.5 to 3.8 wt.% [3, 8, 9, 19]. In the present study, the onset of the first prominent peak of H_2 release occurred at 375 °C, whereas the cited studies reported onset temperatures between 380 and 450 °C, however for coarser powders (particle size 50 – 63 μm) than the one used in this work (particle size < 36 μm). Bhosle et al. [20] and von Zeppelin et al. [21] showed that if the particle size of TiH_2 is reduced by ball milling, which is precisely the method for reducing the particle size of these powders [22], H_2 release starts at lower temperatures.

Hydrogen release from the pre-oxidised TiH_2 yielded a 2 wt.% mass loss, i.e. less than values from 2.3 up to 2.5 wt.% reported for the same oxidation pre-treatment [8 - 10]. This difference can be related to the oxygen content of the powders. For our finer powder the oxygen content increased from 1.4 to 8.7 wt.% during pre-oxidation (Table 1). And the thickness of the resulting oxide layer was about 100 nm (Fig. 7). Matijasevic et al. reported

an increase from 1.0 to 6.0 wt.% O for the same pre-oxidation but on coarser powders. The oxide shell was also 100 nm thick [9]. Our finer powder had a larger surface-to-volume ratio and hence the higher oxygen content. For this, a larger amount of H_2 was sacrificed during pre-oxidation leading later to less mass loss during subsequent heating under Ar flow. The oxide shell acts as an effective diffusion barrier retarding the onset temperature due to the lower diffusivity of H through TiO_2 (rutile) compared to α and β. Calculated diffusion coefficients of H through α and β are 16 and 295 times larger than through TiO_2 at 500°C, and 15 and 139 times larger at 600 °C, respectively, as given in Table 2.

4.2 Phase transformation sequence and core-shell model for as-received TiH_2

4.2.1 Apparent "incompatibilities" between sequence (1) and Ti-H phase diagram

Even though the complete dehydrogenation of δ led to α, as one would expect from the Ti-H phase diagram given in Fig. 9a, two features of sequence (1) are incompatible with the phase diagram. The first one is that at 432 °C, α appeared even though the mass loss was 0.4 % (see Fig. 1) or equivalently, 3.4 wt.% H remained in the solid. This temperature- composition point lies inside the δ field and according to Fig. 9a there should have been only δ. As the temperature further increased and the hydrogen concentration C_H decreased due to H_2 release, not α but β should have appeared. The second apparent incompatibility is that no co-existence of α+β+δ should occur in this eutectoid Ti-H phase diagram, but it was observed.

The reproducibility of sequence (1) was tested by heating two more samples up to 611 and 620 °C, respectively. The first three transformations of sequence (1) and the apparent incompatibilities were reproduced within a scatter of 15 K. The temperatures in sequence (1) differ only slightly from those of a sequence followed in-situ by Matijasevic et al. for coarser TiH_2 powder under He flow by AR-XRD at the experimental station KMC-2, also at BESSY II [23]. We also characterised the sequence for our finer powder by the more surface

sensitive AR-XRD and obtained the same result: α appeared before β and δ+α+β coexisted (Appendix B).

Fig. 9a is the temperature-composition representation for a highly pure solid in equilibrium with 1 bar of pure H_2 gas [16]. Beside the influence of the atmosphere, impurities and heating rate can cause significant deviations from the Ti-H phase diagram [16, 17, 22]. Indeed, by reducing the heating rate from 10 to 5 $K \cdot min^{-1}$, sequence (2), all phase transformations are shifted towards lower temperatures, indicating that the heating rate of 10 $K \cdot min^{-1}$ put the system out of thermodynamic equilibrium.

4.2.2 α before β

Removal of the released H_2 gas from the surrounding atmosphere by the Ar flow was one of the reasons for α appearing before β. Due to Ar flow the initial H_2 partial pressure of the surrounding atmosphere (P_{H2}) was very small, creating a large hydrogen concentration gradient between solid and gas and favouring the formation of the phase with the lowest H solubility. Within the temperature range studied, the H solubility in α (S_H^{α}) is the lowest among the three phases, i.e. $S_H^{\alpha} < S_H^{\beta} < S_H^{\delta}$ (see Fig. 9a). Obviously, α is the phase most compatible with the atmospheric conditions. Besides, the initial oxygen content in the powders (Table 1) and possible oxygen traces in the atmosphere favoured α formation since O is an α stabilizer [18], see Fig. 10a. The larger surface-to-volume ratio of a powder sample compared to a bulk amplified the effect of Ar flow that in turn promoted the α persistence throughout decomposition.

A modification of the atmosphere illustrates the effect of Ar flow. Sequence (3) was obtained by not letting Ar flow. In this experiment, α also appeared prior to β because the initial P_{H2} was zero, but as the decomposition proceeded, P_{H2} of the surrounding atmosphere increased and so the back reaction $H_{2(gas)} \leftrightarrow 2H_{(in\ the\ solid)}$ was enabled. This hindered further

H_2 release as reported by Schonefelder et al. [12]. In sequence (3), α disappeared at 744 °C because P_{H2} was no longer zero and the remaining H in the solid stabilized β up to the maximum temperature. β is a high-temperature phase which in the Ti-H system cannot be retained by natural cooling, hence it transforms into α+δ.

One more example is the phase transformation of TiD_2 under initially resting Ar atmosphere (Appendix C). The applied temperature profile was the same as the one given in Fig. 2b for TiH_2, but much larger TiD_2 samples than TiH_2 were used (3 g vs. 200 mg). Because of a larger sample the back reaction (i.e. the stabilization of β) was established sooner. As a result, the deuteride decomposed less than the hydride and the sequence for TiD_2 was $\delta \xrightarrow{heating} \beta \xrightarrow{cooling} \delta$ and α was not detected at all.

4.2.3 δ+α+β coexistence

The co-existence of α+β+δ even at a reduced heating rate of 5 K·min^{-1} suggests that decomposition was a heterogeneous process either due to a C_H gradient inside the particles and (or) due to a variable P_{H2} depending on the particle position in the sample. The C_H gradient within the particles – lower at the surface in the α shell than in the δ/β core – is linked to the H solubility ranking $S_H^{\alpha} < S_H^{\beta} < S_H^{\delta}$. A variable P_{H2} for different particle positions in the sample might have arisen from a reduced rate of H_2 removal for particles inside the sample compared to particles at the sample surface. In order to evaluate this effect, the phase transformation sequence was also followed by AD-XRD in reflection geometry at and close to the sample surface where H_2 removal was most efficient (Appendix B). In addition, δ+α+β co-existed over a temperature range of 13 K compared to 22 K from sequence (1) referring to the volume. This indicates that P_{H2} still varied depending on the particle position within the thin surface layer probed. But this variation is linked to the volume probed and the corresponding hydrogen concentration profile within.

4.2.4 Core-shell model for as-received powder

In a core-shell model describing the decomposition process of as-received powder, the α phase appearing during heating should form a shell around a δ core and subsequently remain at the surface as discussed in section 4.2.2. Upon further heating, β can be assumed to form an intermediate layer between α and δ consistent with the C_H gradient inside the particles (see section 4.2.3). A temperature-dependent core-shell model is given in Fig. 9b as a radial diagram of phases. In this model, we assume a spherical particle of 3 μm radius (experimental diameter D_{50} = 6 μm) and ignore possible two-phase regions. Volume fractions of phases $f_{vol\,i}$ are calculated as described in Appendix A. In this core-shell representation, the thickness of the α shell initially grows at the expense of the δ core. Later, β appears and grows at the expense of both δ and α. Afterwards, δ disappears and α grows again at the expense of the β core. The superimposed H_2 release curve shows that as the α shell becomes thicker, H_2 release tends to decrease. The main peak of H_2 release starts from about 530 °C when the transition from a δ core into a β core took place, and the α shell reaches a temporary minimum thickness but did not vanish. In this way, the idea suggested previously [10, 23, 24, 29] of α controlling H_2 release is compatible with this model because α has the lowest H solubility among the three phases ($S_H^\alpha < S_H^\beta < S_H^\delta$) and also $D_H^\alpha < D_H^\beta$ (see Table 2). This arrangement of phases is consistent with the TEM investigations (Figs. 4–6) though it ignores the sintering undergone at high temperature. Both the $f_{vol\,i}$ calculation and the H_2 release curve represent an average over a volume containing a large number of particles. But in reality, particles at the surface evolve differently than inside the sample and fine particles should behave differently compared to coarse ones. Nevertheless, the radial diagram reasonably correlates H_2 release with the phase transformation sequence and let visualize the controlling role of α.

4.3 Phase transformation sequence and core-shell model for pre-oxidised TiH_2

4.3.1 Ti_3O transformation into α* and disappearance of the TiO_2 shell

The match between the diffraction lines of Ti_3O and α* is an important feature in the phase transformation of pre-oxidised powder. It occurs because Ti_3O is a superstructure of α*. In Ti_3O, Ti atoms form an hcp arrangement with 1/3 of the octahedral sites orderly occupied by O atoms [25]. However, Ti_3O is stable only up to 500 °C [17] as denoted in the Ti-O phase diagram (Fig. 10a). A dashed arrow indicates that if temperature increases to above the Ti_3O field, the peritectoid transition $Ti_3O \xleftrightarrow{\sim 500\,^{\circ}C} \alpha Ti + Ti_2O$ takes place [17, 18]. Ti_2O is also a superstructure of α* and its principal diffraction lines match those of Ti_3O and α* as well [25]. Above 535 °C the random solid solution of O in Ti, α*, becomes the stable phase. For this reason, we adopted 500 °C as starting temperature for the overall transition from Ti_3O into α* in Fig. 10b.

The O solubility in α* increases above 535 °C and reaches 33 at.% at 600 °C [18]. This influenced another event of the phase transformation: the TiO_2 line in Fig. 3 became less intense from 535 °C and vanished at 623 °C, suggesting that rutile disappeared. It is known from the literature that if TiO_2 reduces its O content the diffraction lines become less intense [26]. As the total O content in the solid did not decrease during heating under Ar (see Table 1), the O concentration profile that before heating had O concentrated at the particle surface (Fig. 7d), evolved to a uniform distribution in α*. It is known that TiO_2 can be reduced by Ti [27]. This process must have initiated around 500 °C where the α* diffraction lines gained intensity, i.e. when $f_{vol\ \alpha^*}$ increased. The point (9.3 wt.% O, 805 °C) taken from Table 1 and Fig. 3, respectively, in Fig. 10a lies inside the α* field, i.e. thermodynamics suggest that only α* as solid product can be expected after complete dehydrogenation.

4.3.2 Core-shell model for pre-oxidised powders

A simplified radial compositional diagram vs. temperature is presented in Fig. 10b for an idealized pre-oxidised TiH_2 particle. Before heating, pre-oxidised TiH_2 particles have three phases arranged in a core-shell structure consisting of a TiO_2 shell, an intermediate layer of Ti_3O and a δ* core. The evolution in temperature of this radial diagram is consistent with the initial core-shell structure, the phase transformation sequence (3) and the complementary TEM investigations on pre-oxidised powder. The field and spatial distribution of Ti_3O and α* are connected due to the transition from Ti_3O into α* at 500 °C. β* is assumed to form an intermediate layer between δ* and α* as in the as-received powder. The thickness of the TiO_2 layer decreases from 535 °C, whereas the α* layer grows not only at the expense of TiO_2 but also of the (δ+β) core until α* becomes the final phase. The superimposed H_2 gas release underlines the controlling role of TiO_2 on H_2 outgassing as its onset coincides with the point at which the TiO_2 shell starts to become thinner, i.e. 535 °C.

4.4 Correlation between contraction of lattice parameter and peaks of H_2 release

Lattice parameters of the phases in as-received and pre-oxidised TiH_2, calculated as described in Appendix A, are given in Fig. 11 jointly with the respective H_2 release curves to emphasize their correlation. The general trend in Fig. 11 is that during isochronal heating the lattice parameters increased due to thermal expansion as long as H_2 release was not prominent and decreased after dehydrogenation had become significant.

Below the onset temperature of the as-received powder (375 °C), a_δ expanded linearly (Fig. 11a). The corresponding linear expansion coefficient of δ between ambient temperature and 375 °C is 10.65×10^{-6} K^{-1} which is in good agreement with the value 10.80×10^{-6} K^{-1} reported by Setoyama et al. [30]. In the following, a_δ contracts in two regimes correlated with two peaks of H_2 release. Similarly, the main H_2 release peak results in a monotonic contraction of a_β.

In contrast, c_α expands temporarily between 500 and 550 °C. This could be due to an increase in the oxygen concentration in the α shell. Since in this period the α shell becomes thinner (see Fig. 9b), and the total oxygen content of the sample does not decrease (see Table 2), the α shell becomes richer in O because α remains the preferred host for O [28]. Another effect contributing to the expansion of c_α is the slight S_H^α increase above 300 °C (see Fig. 9a) [16]. This argument is also valid for a_α but the occupancy of either tetrahedral sites by H or octahedral sites by O modifies preferentially the distance between c planes in α which in turn affects more significantly c_α than a_α [16, 18]. After this period, between 550 and 710 °C, c_α contracts during the strongest dehydrogenation stage. In fact, a_α contracts up to 740 °C, after which both a_α and c_α expanded, indicating the dominance of thermal expansion over lattice contraction.

For the pre-oxidised sample, the lattice parameters a_{α^*} and c_{α^*} of the hcp α* phase that were calculated for the whole temperature range represent below 500 °C, fractions of the lattice parameters of Ti_3O determined by the expressions: $a_{Ti_3O} = \sqrt{3} \cdot a_{\alpha^*}$ and $a_{Ti_3O} = 2 \cdot c_{\alpha^*}$ [25]. Thus, the distinction done in Fig. 11 b between Ti_3O and α* is in order to be consistent with the assumed transition from Ti_3O into α* at 500 °C discussed in section 4.3.1. The smaller initial a_{δ^*} compared to a_δ comes from the lower initial hydrogen content [16]. In contrast to a_δ, the initial expansion of a_{δ^*} is nonlinear. The expansion of a_{δ^*} in this pre-oxidised sample is shifted by 160 K up to 535 °C with respect to the as-received one, in analogy to the shift of the onset of H_2 release. The more modest contraction of a_{δ^*} and a_{β^*} above 535 °C compared to their isomorphic a_δ and a_β is due to the lower total H_2 released from the pre-oxidised powder. Same as in the as-received powder a_{α^*} contracts further than c_{α^*} in the pre-oxidised sample.

The difference in absolute values between the lattice parameters of α and α* above 650 °C suggests that the smaller c_α and a_α more efficiently restricted H_2 outgassing than $c_{\alpha*}$ and $a_{\alpha*}$. This could explain the faster decay and exhaustion of hydrogen above 650 °C from the pre-oxidised powder controlled by a relatively thick α* shell compared to the thinner α shell covering the as-received powder (compare Figs. 9b and 10b above 650 ° C). Additionally, the higher the O content, the more the hcp structure is stabilized [18]. Due to the initial oxide layer, the pre-oxidised powder remains a loose powder after cooling from 805 °C (see Fig. 8a) which does not affect the effectiveness of H_2 removal, whereas the as-received powder undergoes some interparticle sintering and compaction (see Fig. 6a) which delayed the final stages of dehydrogenation.

5. Summary

The phase transformation sequences of both as-received and pre-oxidised TiH_2 powders were correlated with the observed peaks of H_2 release. The sequence of dehydrogenation for pre-oxidised TiH_2 was reported for the first time. For heating at 10 $K \cdot min^{-1}$ under flowing Ar we found only thermal expansion and nearly no H_2 release up to 375 °C in the as-received powder and 535 °C in the pre-oxidised one. Upon further temperature increase, with every peak of H_2 release the lattice parameters contracted.

Based on complementary TEM analysis we validated experimentally core-shell models for describing the heterogeneous decomposition processes of both as-received and pre-oxidized TiH_2 powders. These models imply the presence of an α shell controlling H_2 outgassing from the as-received TiH_2 powder, whereas a TiO_2 rutile shell controls the outgassing from the pre-oxidised TiH_2 powder.

The flow conditions during heating were shown to be essential by carrying out various experiments at different conditions in which the evolving hydrogen was either removed

continuously stabilizing α or allowed to form a surrounding hydrogen atmosphere that stabilized β at the maximum temperature.

Acknowledgements

We thank M. Mukherjee, Ch. Abromeit, N. Wanderka, S. Klaumünzer and Ch. Genzel for constructive discussions, Ch. Förster for helping with TEM sample preparation and H. Kropf with SEM. O. Goerke from TU Berlin assisted the oxygen content analysis.

6. References

[1] Banhart J. Prog Mater Sci 2001; 46: 559.
[2] Erk KA, Dunand DC, Shull KR. Acta Mater 2008; 56: 5147.
[3] Liu H, He P, Feng JC, Cao J. Int J Hydrogen Energy 2010; 34: 3018.
[4] Duarte I, Banhart J. Acta Mater 2000; 48: 2349.
[5] Matijasevic B, Banhart J. Scripta Mater; 2006:54; 503.
[6] Gergely V, Clyne TW. Adv Eng Mater 2000; 2: 175.
[7] Kennedy AR. Scripta Mater 2002; 47: 763.
[8] Lehmhus D, Rausch G. Adv Eng Mater 2004; 6: 313.
[9] Matijasevic-Lux B, Banhart J, Fiechter S, Görke O, Wanderka N. Acta Mater 2006; 54: 1887.
[10] Malachevsky MT, D'Ovidio C. Scripta Mater 2009; 61: 190.
[11] Sandim HRZ, Morante BV, Suzuki PA. Mater Res 2005; 8: 293.
[12] Schoenfelder CW, Swisher JH. J Vac Sci Technol 1973; 10: 862.
[13] Gruner W J. Analytical Chem 1999; 365: 597.
[14] Genzel Ch, Denks I, Gibmeier J, Klaus M, Wagener G. Nucl Instr and Meth in Phys Res A 2007; 578: 23.
[15] Denks I, Genzel Ch. Nucl Instr and Meth in Phys Res B 2007; 262: 87.
[16] San Martin A and Manchester FD. Bull Alloy Phase Diag 1987; 8: 30.
[17] Kubaschewski-von Goldbeck O. *Phase diagrams*, in: Komarek (Ed.). *Titanium: physico-chemical properties of its compounds and alloys.* Vienna: IAEA; 1983.
[18] Landolt-Börnstein New Series IV/5 MSIT® *"O-Ti (Oxygen-Titanium)"* New York: Springer Materials; 2005.

[19] Proa-Flores PM, Drew RLA. Adv Eng Mater 2008; 10: 830.
[20] Bhosle V, Baburaj E G, Miranova M, Salama K. Mater Sci Eng A 2003; 356: 190.
[21] von Zeppelin F, Hirscher M, Stanzick H, Banhart J. Compos Sci Technol 2003; 63: 2293.
[22] Müller WM. *Titanium Hydrides*, in: Müller WM, Blackledge JP, Libowitz GG (Eds.). *Metal hydrides*. New York: Academic Press; 1968.
[23] Matijasevic B. PhD Thesis, Technische Universität Berlin; 2006.
[24] Takasaki A, Furuya Y, Ojima K, Taneda Y. J Alloys Comp 1995; 224: 269.
[25] Kornilov II, Vavilova VV, Fykin LE, Ozerov RP, Solowiev SP, Smirnov VP. Met Trans 1970; 2: 2569.
[26] Meyer RJ, Pietsch EHE. *Gmelins Handbuch der Anorganischen Chemie: Titan Vol 41* Weinheim: Verlag Chemie; 1951.
[27] Wiberg E, Wiberg N, Holleman AF. *Holleman-Wiberg Inorganic Chemistry, 34th ed*. New York: Academic Press; 2001.
[28] Schlapbach L. *Surface properties and activation*, in: Schlapbach L (Ed.). Hydrogen in Intermetallic Compounds II. Berlin Hidelberg New York: Springer-Verlag; 1992.
[29] Swisher JH. Sandia Laboratories Report No. SCL-RR-720059; 1972.
[30] Setoyama D, Matsunaga J, Muta H, Uno M, Yamanaka S. J Alloys Comp 2004; 381: 215.
[31] Cullity BD. *Elements of X-Ray Diffraction*. Reading; Addison-Wesley: 1978.
[32] Hill GJ. Brit J Appl Phys (J Phys D) 1968; 1: 1151.
[33] http://www.helmholtz-berlin.de/userservice/neutrons/instrumentation /neutron-instruments/e6_en.html
[34] Kubaschewski O, *Diffusion*, in Komarek (Ed.). *Titanium: physico-chemical properties of its compounds and alloys.* Vienna: IAEA; 1983.
[35] Laine ESU. J Phys F: Metal Phys 1978; 8: 1343.
[36] Matzke HJ, Rondinella VV. *Diffusion in carbides, nitrides, hydrides and borides*, in: Beke DL (Ed.). Landolt-Börnstein - Group III/Vol 33B1, New York: Springer Materials; 2010.

Appendix A – ED-XRD data analysis

In ED-XRD diffraction, lines are detected at particular energies E_{hkl} since the diffracted photon energies obey Bragg's law, which reads in its energy-dispersive form as $E_{hkl} = hc/2d_{hkl}\sin\theta$ (A.1), where h is Planck's constant and c the speed of light. We evaluated data with a self-developed tool that runs under the software package `Mathematica` [14, 15]. Different diffraction lines were fitted by Gaussians, which allowed for calculating integrated intensities. d_{hkl} values were obtained by evaluating Eq. (A.1) for the diffraction lines δ_{220}, β_{200}, α_{101}, α_{102} and r_{101} (of TiO_2). These lines do not overlap with other lines and allow for calculating volume fractions of phases $f_{vol,i}$, with i = δ, δ*, α, α*, β, β*, Ti_3O and TiO_2, by dividing the integrated intensity of the principal line I_i by the summed integrated intensity I_{sum} of the principal lines of all the phases present at a given temperature. Each volume fraction was given by the relation, $f_{vol,i} = I_i/I_{sum}$. I_α and I_{α^*} were directly obtained from the principal lines α_{101} and α^*_{101}. The latter was considered o_{112} (belonging to Ti_3O) below 500 °C thus rendering I_{Ti_3O}. For the δ and δ* phases, we integrated the lines δ_{220} and δ^*_{220} whose fractional relative intensity is 0.57 with respect to the principal line. Therefore we assumed $I_{\delta\ or\ \delta^*} = I_{\delta_{220}\ or\ \delta^*_{220}}/0.57$. Likewise, $I_{\beta\ or\ \beta^*} = I_{\beta_{200}\ or\ \beta^*_{200}}/0.15$ and $I_{TiO_2} = I_{r_{101}}/0.57$. The Mathematica tool has a module to quantify f_{vol} in samples containing only two phases based on Ref. [35]. Since our samples contained up to four phases, we made this simplified calculation, which was sufficient for deducing temperature dependencies for all $f_{vol,i}$.

Lattice parameters a_δ and a_β of the cubic phases δ and β, respectively, were calculated from $1/d_{hkl,i}^{\,2} = h^2 + k^2 + l^2/a_i^{\,2}$ and those of the hexagonal phase α, a_α and c_α, from $1/d_{hkl,i}^{\,2} = 4/3\left(h^2 + hk + k^2/a_i^{\,2}\right) + l^2/c_i^{\,2}$ [31]. By evaluating the fitted lines δ_{220}, β_{200}, α_{101}, and α_{102} we obtained $a_\delta = 8\cdot d_{220,\delta}$, $a_\beta = 4\cdot d_{200,\beta}$, $a_\alpha = d_{101,\alpha}\cdot d_{102,\alpha}\Big/\sqrt{d_{102,\alpha}^{\,2} - d_{101,\alpha}^{\,2}/4}$,

and $c_\alpha = \sqrt{3} \cdot d_{101,\alpha} \cdot d_{102,\alpha} \Big/ \sqrt{{d_{101,\alpha}}^2 - {d_{102,\alpha}}^2}$. Finally, d_{hkl} values obtained from Rietveld-refined lattice parameters of δ and δ* (from AD-XRD data, section 2.3 and 3.1) were used for adjusting systematic offsets E_{hkl} peaks measured by ED-XRD of both as-received and untreated samples via the relation (A.1).

Appendix B – Phase transformation TiH_2 followed in-situ by AD-XRD

The phase transformation sequence of as-received TiH_2 was followed in-situ also in reflection geometry at the KMC-2 experimental station at BESSY II of the Helmholtz Centre Berlin. AD-XRD in reflection allowed to assess surface-specific effects. For this, a 2D detector covered a 2θ-window of 15 ° and acquired one diffractogram every 11 seconds, yielding a temperature resolution below 2 K. The powder was cold-pressed to tablets of 6 mm diameter and 1 mm thickness. A photon-energy of 8 keV provided about 11 μm penetration depth through Ti thus limiting detection of diffracted intensities to the surface region. A cavity was drilled into the sample surface to accommodate a thermocouple beside the beam path. The tablet was fastened to a resistive heater. A stainless steel dome with X-ray transparent Kapton windows sealed a chamber during isochronal heating at 10 $K \cdot min^{-1}$ under Ar flow.

Fig. B.1 displays the angle-dispersive diffracted intensities vs. time during heating up to 808 °C. The starting phase was δ, then α appeared at 440 °C and β at 465 °C. The δ phase disappeared at 478 °C and β at 620 °C. So δ+α+β coexisted for 13 K. Two additional weak diffraction lines arose from Ti_3O and TiO_2 as marked in Fig. B.1. Oxidation at the sample surface probably occurred because α acted as a getter of residual oxygen in the chamber [28].

Ignoring these oxides, the phase transformation sequence was:

$$\delta \xrightarrow{440\,°C} \delta + \alpha \xrightarrow{465\,°C} \delta + \alpha + \beta \xrightarrow{478\,°C} \alpha + \beta \xrightarrow{620\,°C} \alpha \qquad \text{(B1)}$$

This is the same sequence as (1) and (2) but with differing temperatures.

Appendix C – Phase transformation of TiD_2 followed in-situ by neutron diffraction

The phase transformation of TiD_2 was also followed in-situ by neutron powder diffraction in transmission mode at the diffractometer E6 of the Helmholtz Centre Berlin. Neutrons of 0.24 nm wavelength and an area detector fixed at $2\theta = 62$ ° were used to perform in-situ diffraction at varying temperature within a 2θ-window of 15.5 degrees (see [33] for further details of the diffractometer). TiD_2 instead of TiH_2 was used to reduce incoherent scattering from hydrogen and to reduce background noise. 3 g of as-received TiD_2 powder (custom made by GfE, Nüremberg) was poured into a quartz tube of 1 mm diameter, which was connected to a gas-tight recipient of 20 litres capacity to limit the pressure increase due to decomposition of TiD_2. A valve kept the gas pressure below 1.2 bar. The system was evacuated to 10^{-6} mbar using a turbo-pump, and subsequently back-filled with Ar. The quartz tube was positioned inside a furnace with open paths for incoming and diffracted neutrons. At 348 and 897 °C full 2θ-scans were performed (Fig. C.1a). From 348 to 897 °C, the sample was heated at 10 $K \cdot min^{-1}$ and the phase transformation sequence was followed inside the marked 2θ-window with 20 K temperature resolution. Diffracted peaks marked with C in Fig. C.1b originated from the quartz tube as verified by a reference measurement on the empty tube. The starting phase at 348 °C was δ, which transformed between 633 and 656 °C into β that remained up to 897 °C. After cooling down to 277 °C, δ was again the only phase present, i.e. the sequence was $\delta \xrightarrow{heating} \beta \xrightarrow{cooling} \delta$. The α phase was not detected.

Neutron diffraction as ED-XRD allowed for following changes in the bulk of the sample. However, the time resolution of 2 minutes was not enough to replace ED-XRD.

Captions and tables

Fig. 1 – Specific mass = 2 ion current I_2 and mass loss Δm vs. temperature for as-received and pre-oxidised TiH_2 powders heated at 10 $K \cdot min^{-1}$ in flowing Ar.

Fig. 2 – Density maps of diffracted intensities (colour scale) dispersed in energy (in keV) vs. time (in minutes) show the evolution of the δ, β and α diffraction lines in as-received powder while applying the temperature profile $T_H(t)$ under: a) flowing Ar and b) resting Ar plus the released H_2. Number triples are (hkl) indices. Legends connected to the measured sample temperature profile $T_S(t)$ indicate corresponding figure and sample condition for TEM investigations.

Fig. 3 – Same as Fig. 2a but for pre-oxidised TiH_2 powder. Peaks of Ti_3O and TiO_2 are indicated by o and r, respectively. The symbol "*"refers to the compositional modification after pre-oxidation, but δ*, β* and α* are structurally isomorphous to δ, β and α.

Fig. 4 – a) SEM image shows the morphology of as-received powder. b) ZLFBF image and SAED pattern for the visible area. The fully indexed sequence of diffraction rings confirms that δ-TiH_2 phase is the only phase present in this sample.

Fig. 5 – a) ZLFBF image of an as-received TiH_2 particle after heating to 430 °C and cooling (see also Fig. 2a). b) Indexed SAED pattern obtained from the indicated region giving evidence of an α-phase shell. c) SAED from the core corresponds to a [200] zone axis of the δ phase.

Fig. 6 – a) SEM image of as-received TiH_2 after heating to 807 °C and cooling, showing sintering of the powder particles, porosity and grain coarsening. b) ZLFBF image in which

triple points of grain boundaries are indicated by arrows. Diffraction pattern corresponds to the [110] zone axis of the α phase.

Fig. 7 – Spatial distribution of phases in pre-oxidised TiH_2 "before heating" (i.e. the state indicated in Fig. 3) as investigated by TEM. a) ZLFBF image of a particle slice. b) SAED pattern from the core region showing the [211] zone axis of the δ* hydride. c) SAED pattern of the shell region, where the main diffracting phases were identified as Ti_3O and TiO_2. d) Grey-scale oxygen map of the same area. Lighter grey in the shell indicates oxygen enrichment.

Fig. 8 – a) SEM image of a pre-oxidised TiH_2 particle after heating to 805 °C and cooling, see Fig. 3. b) ZLFBF image showing the outer region of one particle on which SAED was obtained. The SAED pattern shows the zone axis [002] of the hcp α* phase.

Fig. 9 – a) Phase diagram of Ti-H system adapted from Ref. [16]. 3.5 wt.% H at 432 °C corresponds to the mass loss of 0.4 % indicated in Fig. 1. The arrow entering the δ+β field is discussed in the text. b) Radial distribution of phases vs. temperature applying a core-shell model assuming a spherical particle on the f_v volume fractions of phases. The H_2 release curve (same as in Fig. 1) is superimposed.

Fig. 10 – a) Ti-rich part of the O-Ti binary phase diagram adapted from Ref. [18]. Dashed arrows and particular temperature and compositions are discussed in the text. b) Idem Fig. 9b but for a pre-oxidised particle.

Fig. 11 – Lattice parameters of δ, β, α for a) as-received TiH_2 and b) δ*, β*, α* and Ti_3O for pre-oxidised TiH_2 vs. temperature. The curves of H_2 release and particular temperatures (from Fig. 2a and 3) are superimposed.

Fig. B.1 – Density map of diffracted intensities of as-received TiH_2 vs. time for the temperature profile $T_s(t)$ analogous to Fig. 2a but dispersive in 2θ and in reflection geometry using a photon energy of 8 keV.

Fig. C.1 – a) 2θ scans performed by neutron diffraction (λ = 0.24 nm) on TiD_2 show δ-phase at 348 °C, β after heating till 897 °C and again δ after cooling down to 277 °C. Peaks labelled by C arise from tube containing TiD_2 powders. b) Phase transformation $\delta \rightarrow \beta$ during heating.

Table(s)

Table 1 – Measured oxygen content of TiH_2 powder samples

	Oxygen content, in wt.%	
	before heating *	after cooling *
As-received	1.4	1.7
Pre-oxidised	8.7	9.3

(*) Indicated in Fig. 2a for as-received and in Fig. 3 for pre-oxidised samples.

Table 2 – Calculated diffusion coefficients of H through β, α and TiO_2 at 500 and 600 °C

Diffusion coefficients(**)	500 °C	600 °C	Ratio $D_H^{\beta \text{ or } \alpha} / D_H^{TiO_2}$ at 500 °C, at 600 °C	Ref.
D_H^{β}, $cm^2.s^{-1}$	7.56×10^{-5}	9.87×10^{-5}	295 , 139	[36]
D_H^{α}, $cm^2.s^{-1}$	4.05×10^{-6}	1.06×10^{-5}	16, 15	[34]
$D_H^{TiO_2}$, $cm^2.s^{-1}$	2.56×10^{-7}	7.06×10^{-7}	__	[32]

(**) calculated using pre-exponential factors and activation energies from the indicated references assuming an Arrhenius law.

Figure1

Click here to download high resolution image

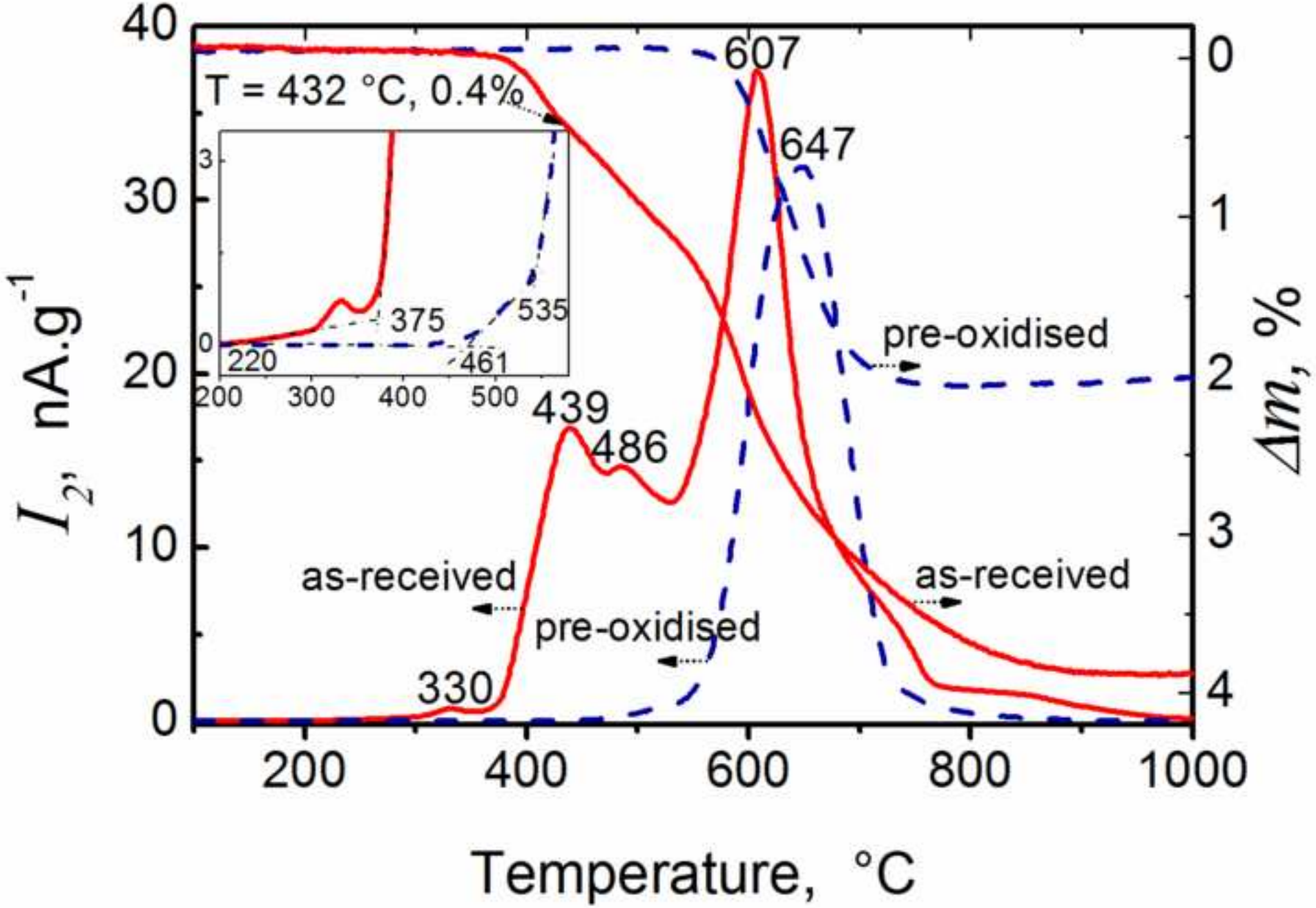

Figure2a

Click here to download high resolution image

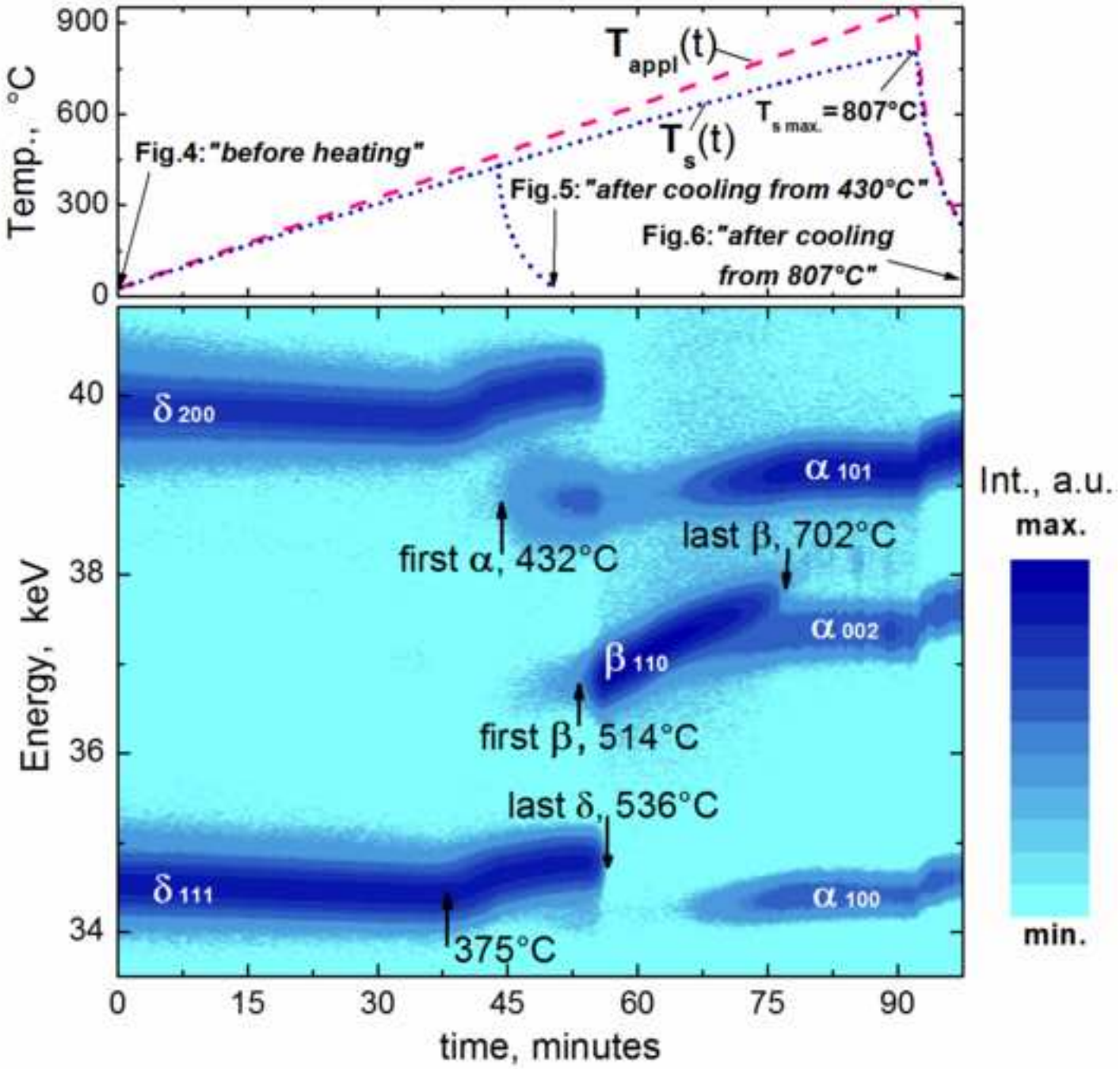

a) as-received (flowing Ar)

Figure2b

Click here to download high resolution image

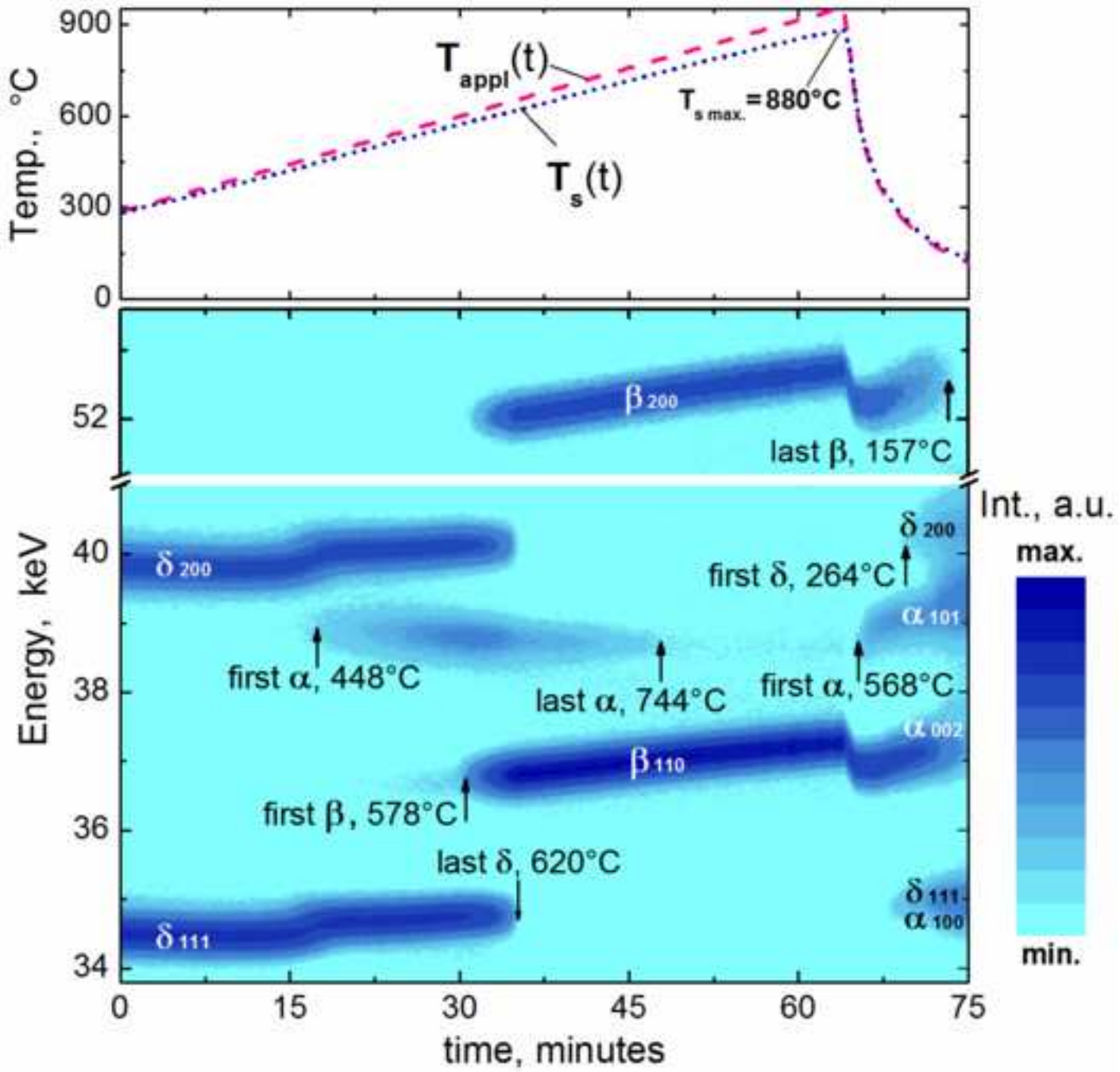

b) as-received (resting Ar+released H_2)

Figure3

Click here to download high resolution image

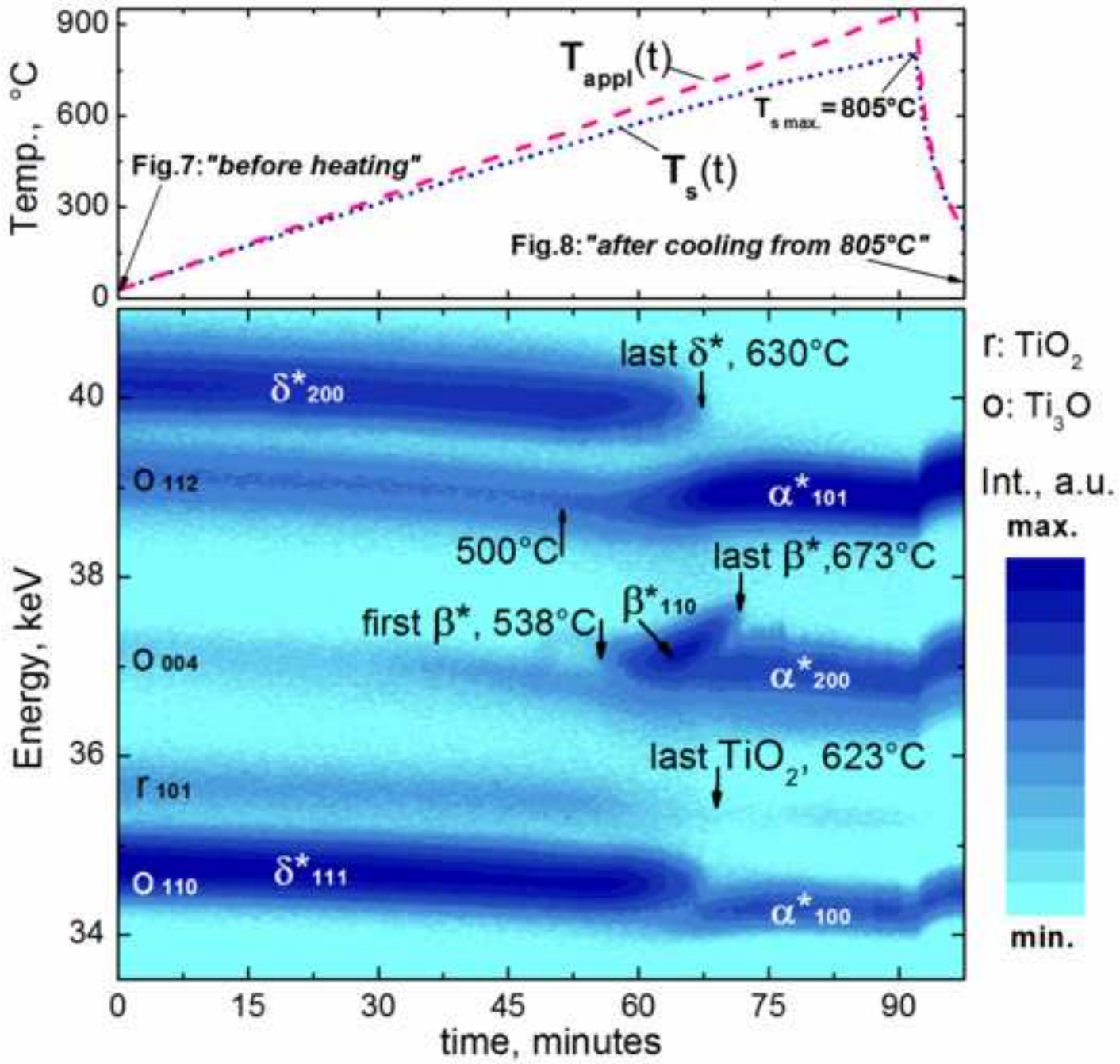

pre-oxidised (flowing Ar)

Figure4

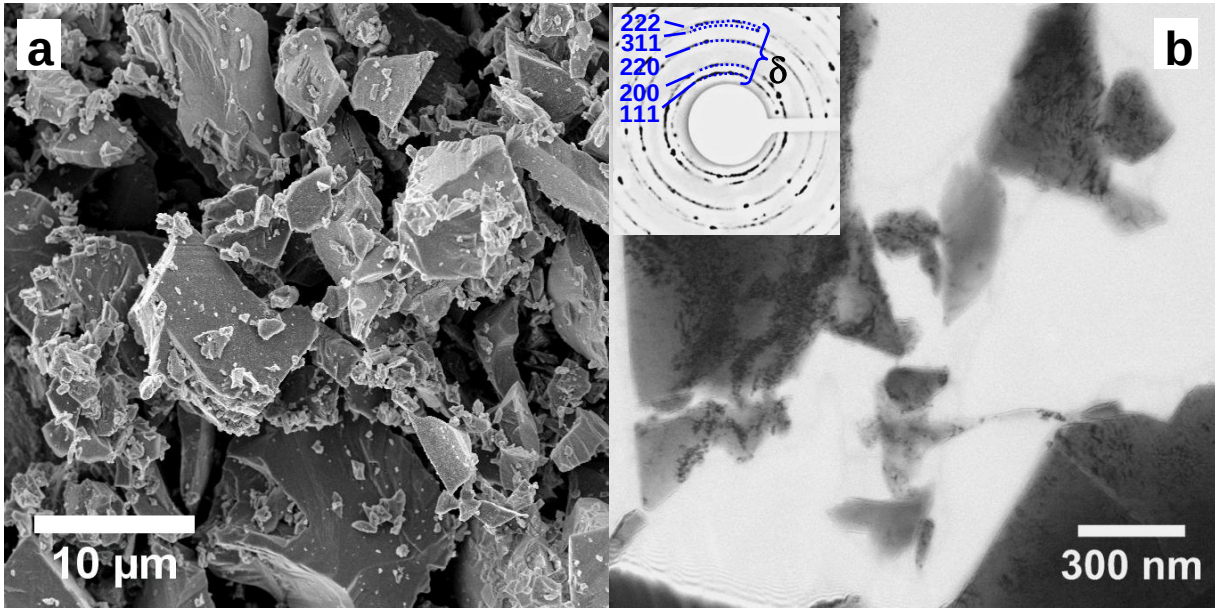

Figure5

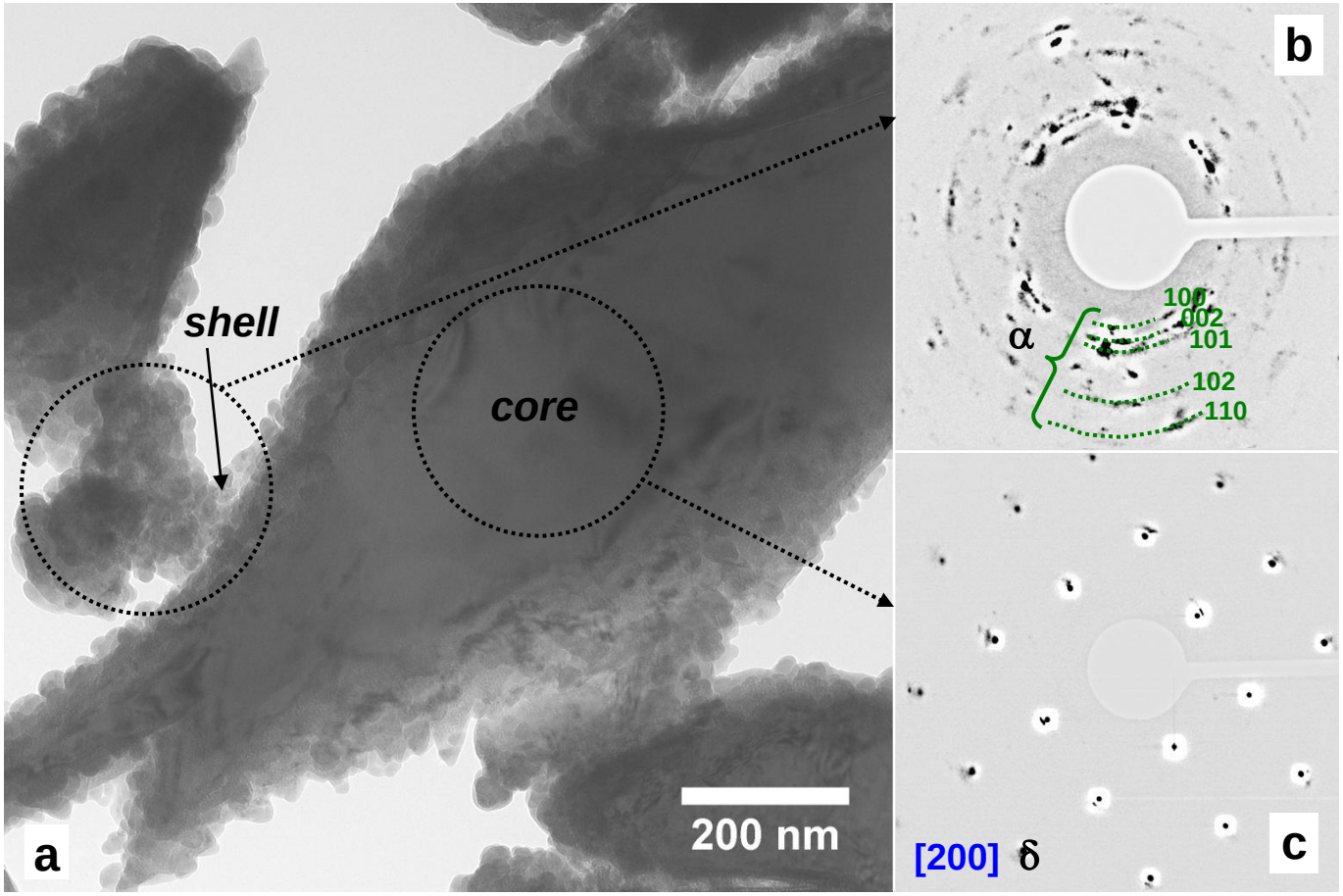

Figure6

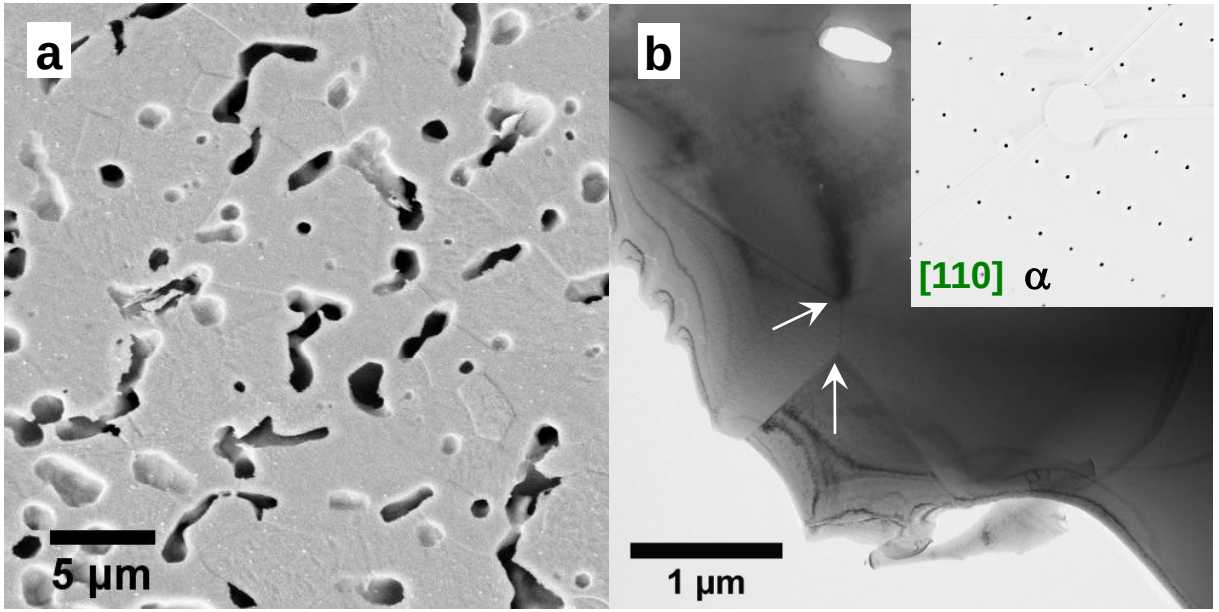

Figure7

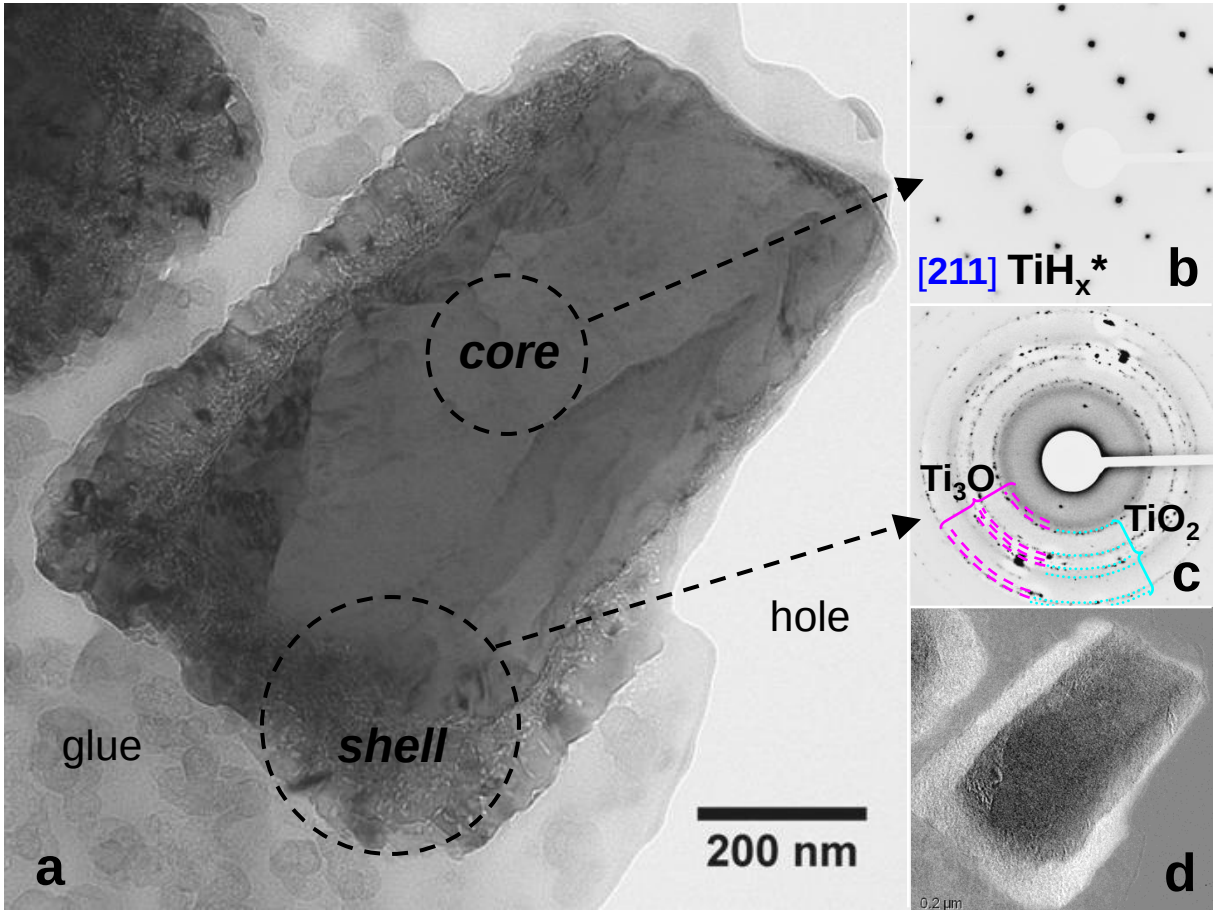

Figure8

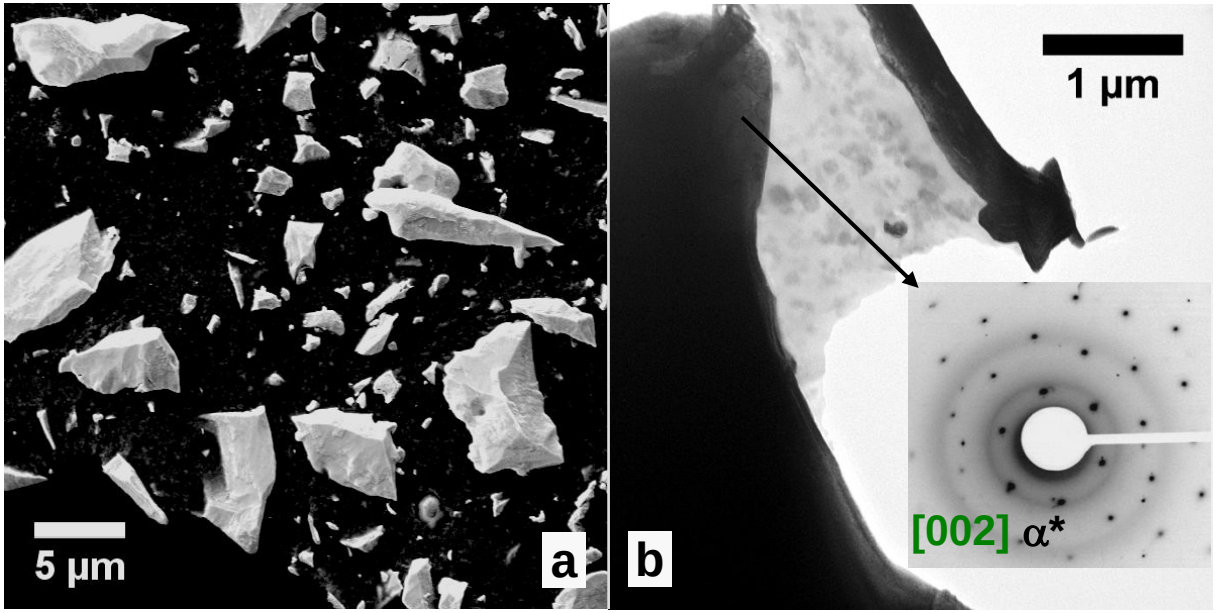

Figure9a

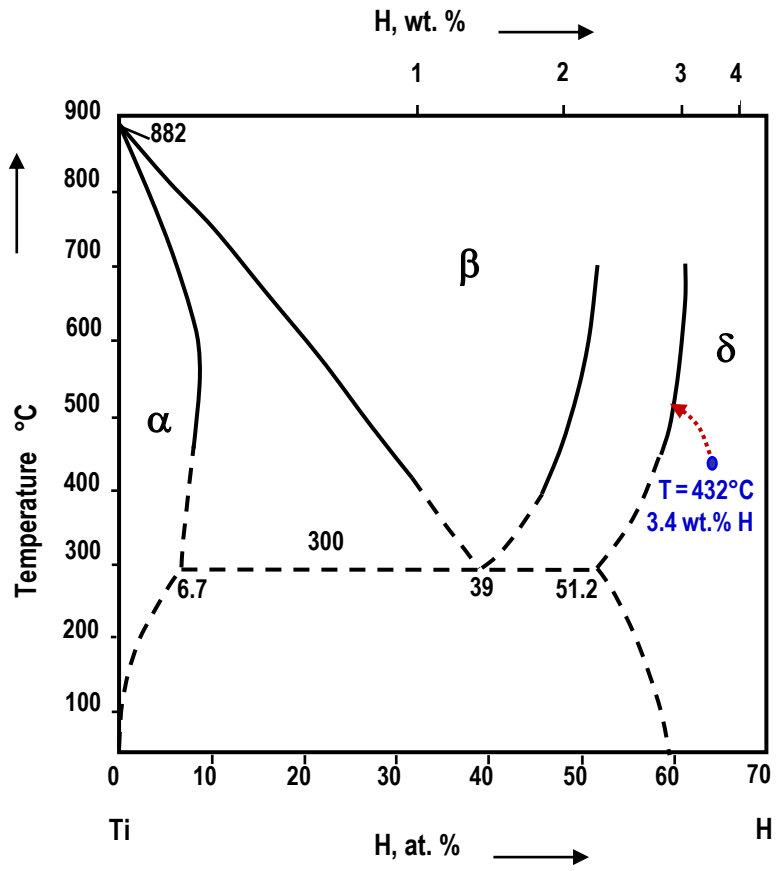
H, wt. %
1
2
3
4
900
800
700
600
500
400
300
200
100
882
β
δ
α
Temperature °C
T = 432°C
3.4 wt.% H
300
6.7
39
51.2
0
10
20
30
40
50
60
70
Ti
H
H, at. %

Figure9b

Click here to download high resolution image

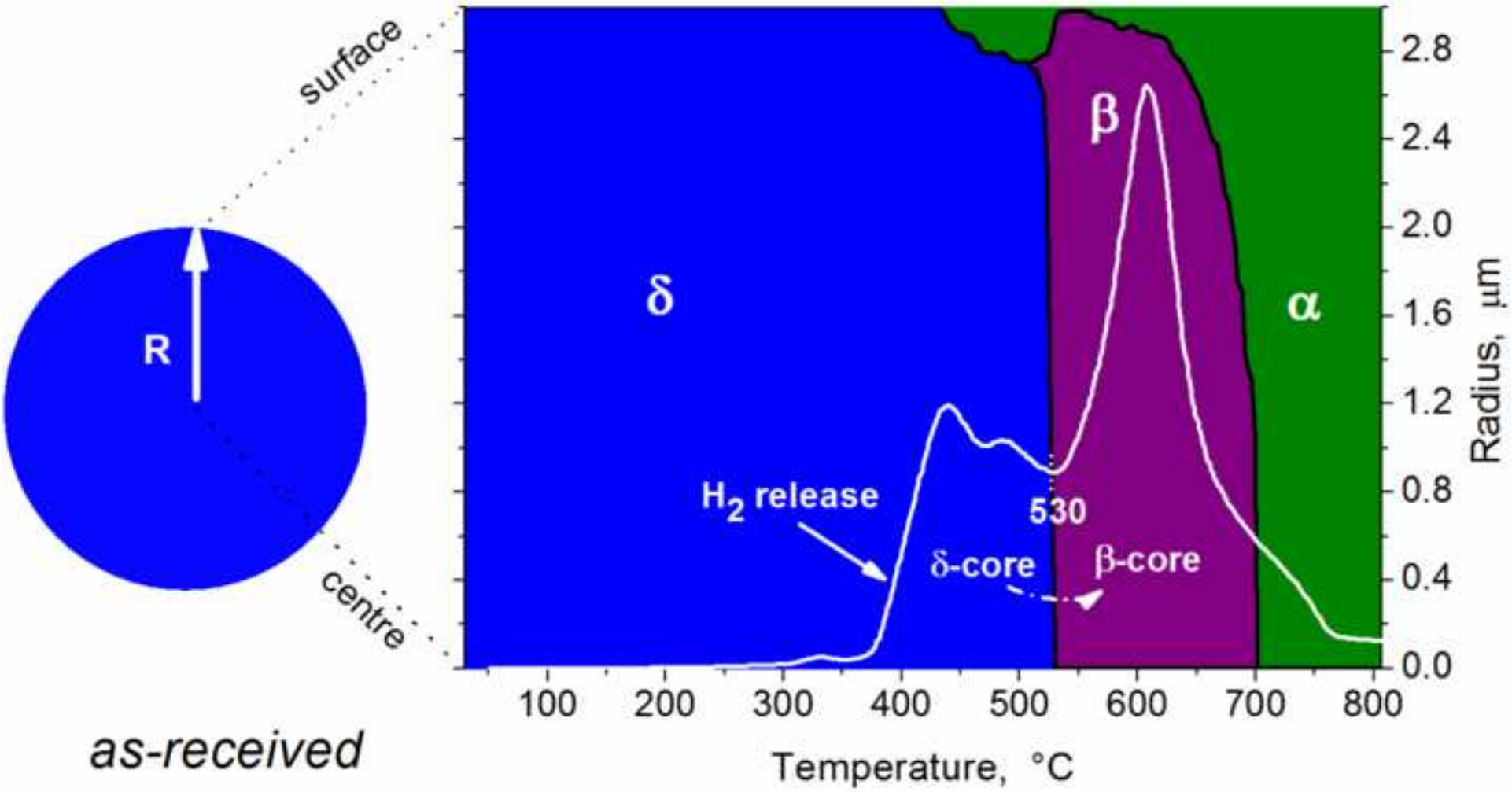

Figure10a

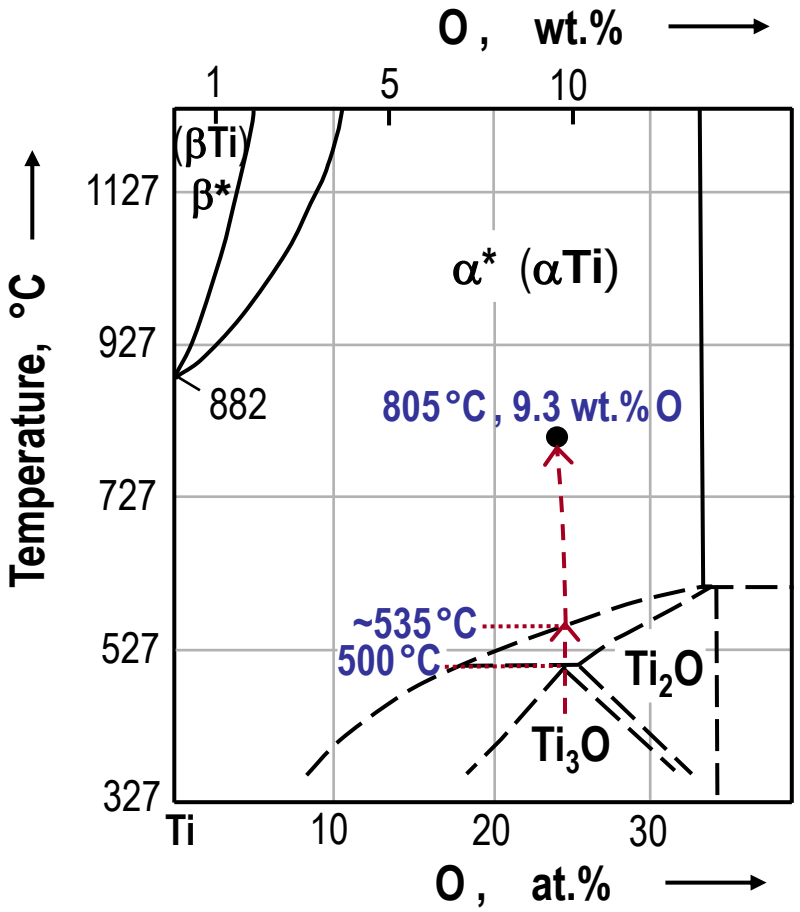
O , wt.%
1
5
10
(βTi)
β*
1127
927
882
α* (αTi)
805 °C , 9.3 wt.% O
727
~535 °C
500 °C
527
Ti2O
Ti3O
327
Ti
10
20
30
O , at.%
Temperature, °C

Figure10b

Click here to download high resolution image

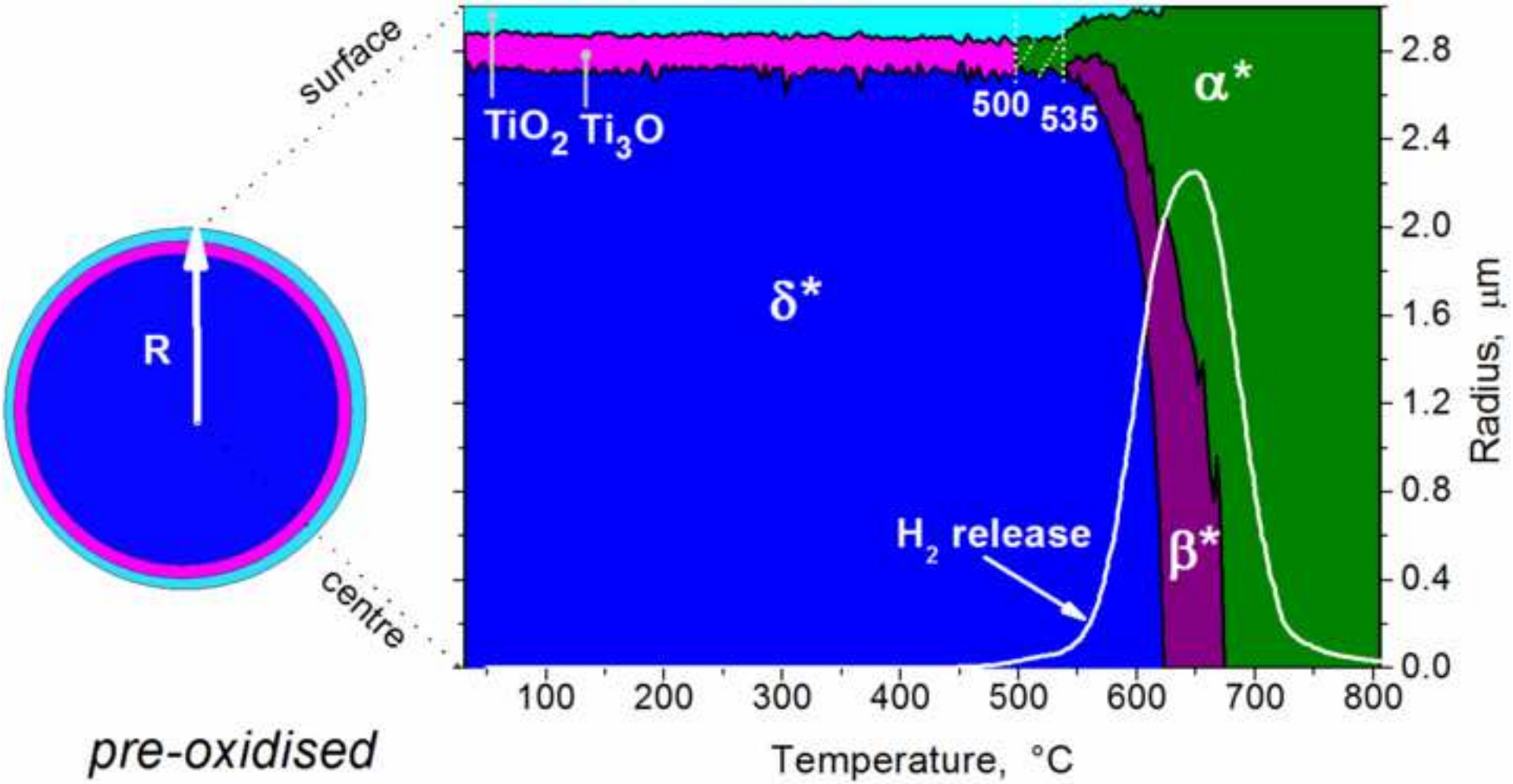

Figure11a

Click here to download high resolution image

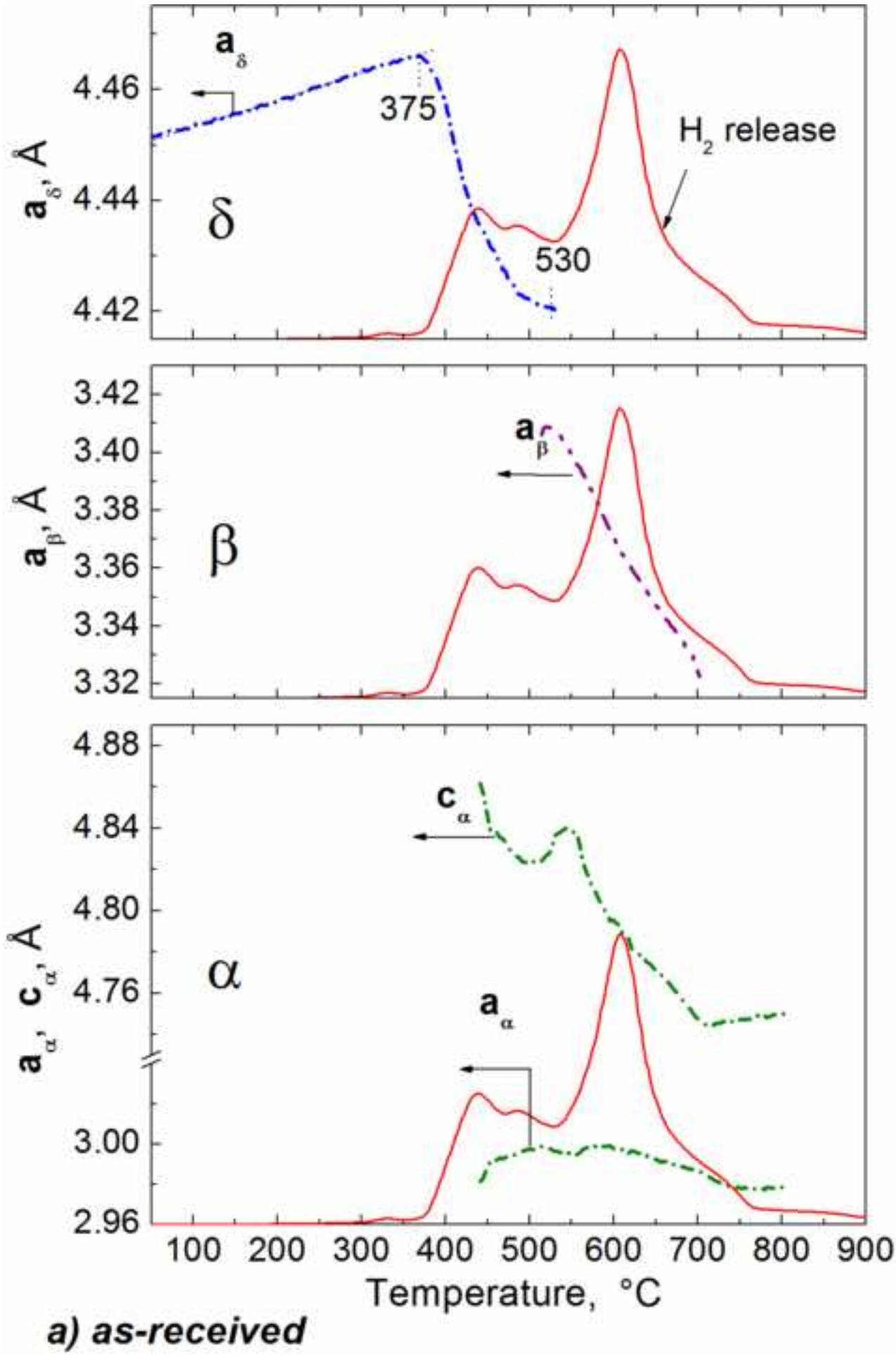

a) as-received

Figure11b

Click here to download high resolution image

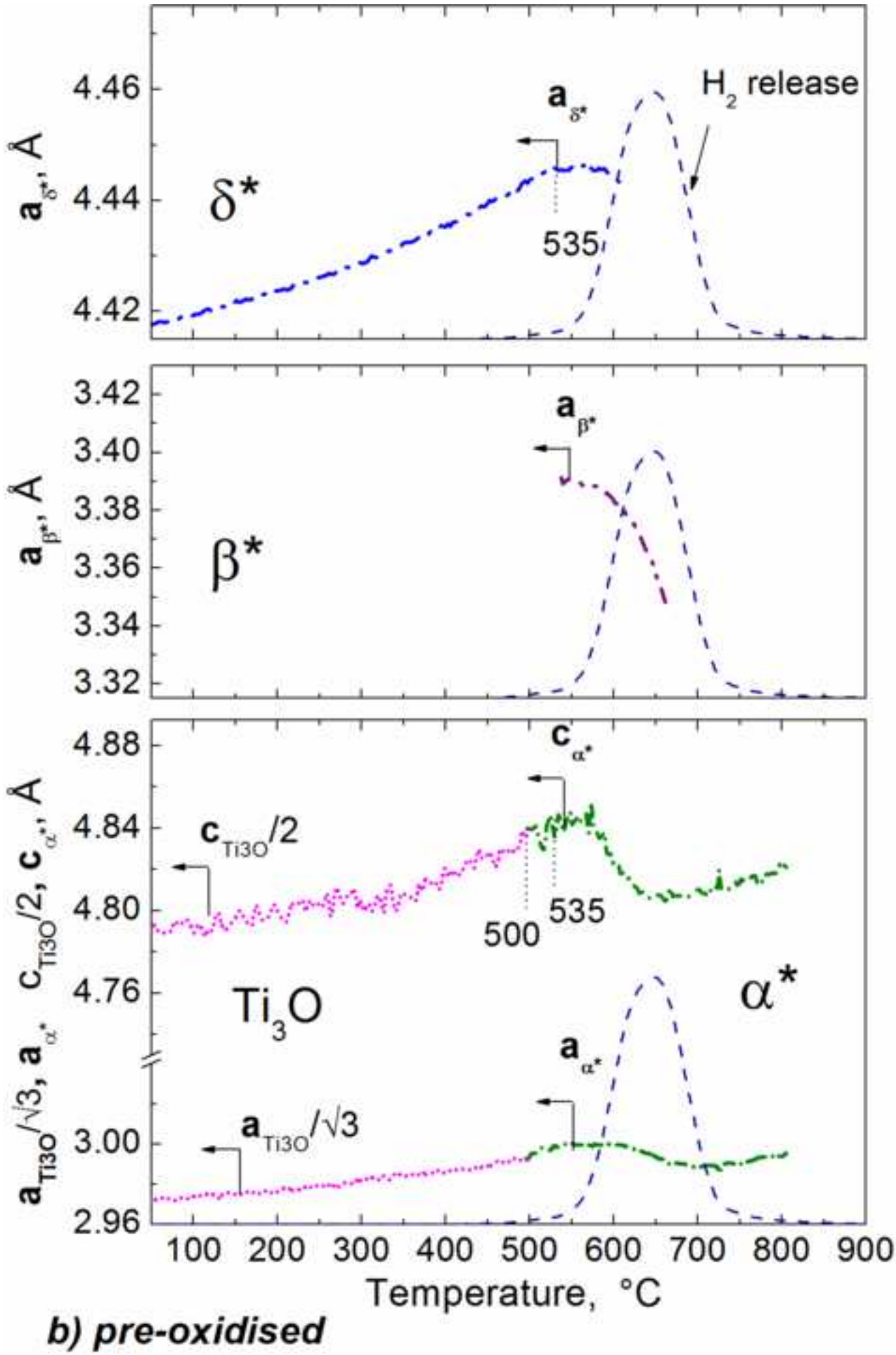

b) pre-oxidised

FigureB1

Click here to download high resolution image

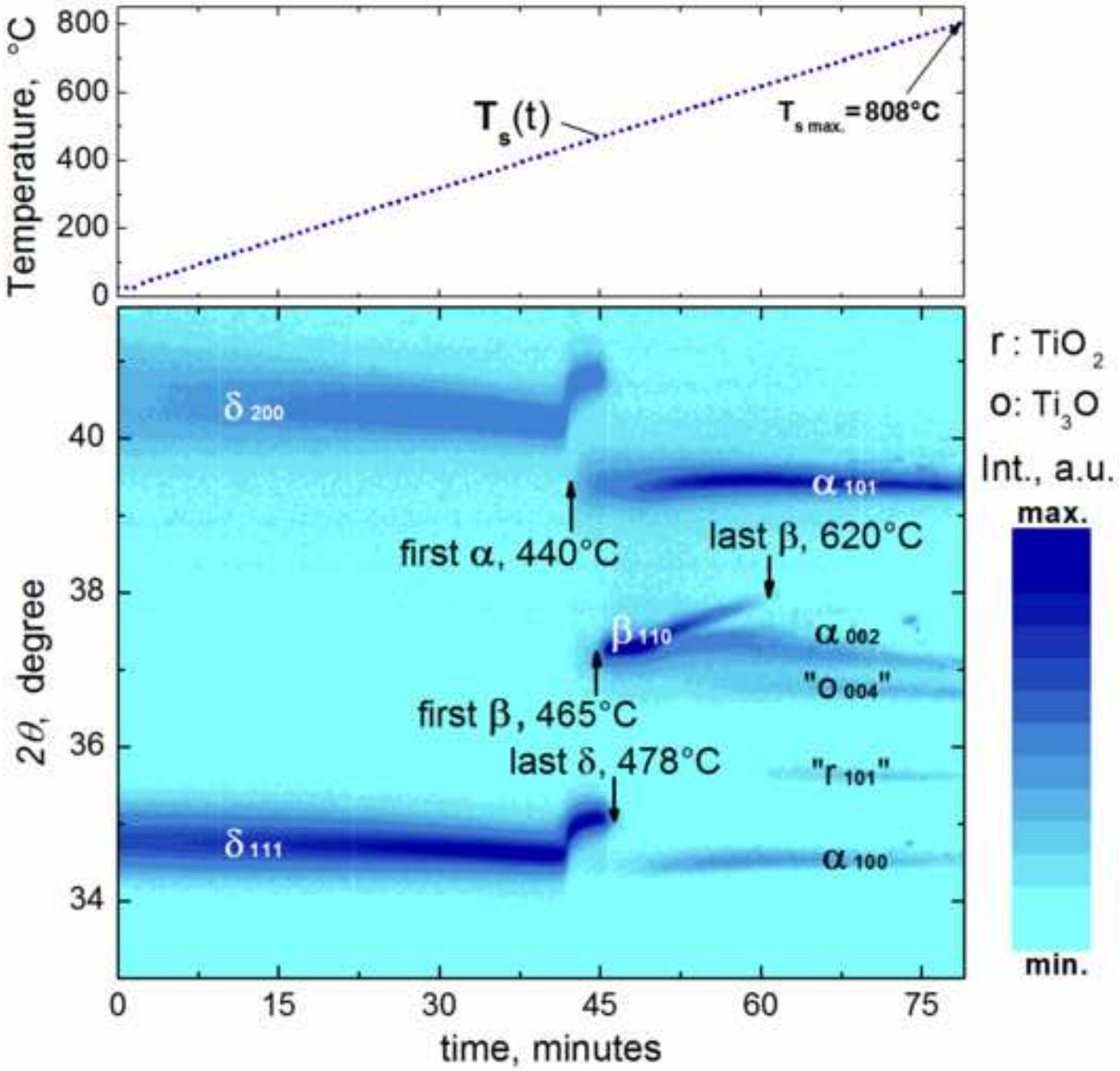

FigureC1

Click here to download high resolution image